PAPER • OPEN ACCESS

Impact of Yacora evaluated molecular effective rate coefficients on detached SOLPS-ITER simulations

To cite this article: J. Bryant *et al* 2025 *Nucl. Fusion* **65** 036025

OPEN ACCESS
IOP Publishing | International Atomic Energy Agency
Nuclear Fusion
Nucl. Fusion **65** (2025) 036025 (16pp)
https://doi.org/10.1088/1741-4326/adb3bb

Impact of Yacora evaluated molecular effective rate coefficients on detached SOLPS-ITER simulations

J. Bryant[1,*], K. McKay[1], J.R. Harrison[2], D. Moulton[2], K. Verhaegh[2], C. Cowley[3], R.C. Bergmayr[4], U. Fantz[4] and D. Wünderlich[4]

[1] Department of Electrical Engineering and Electronics, University of Liverpool, Liverpool L69 3GJ, United Kingdom of Great Britain and Northern Ireland
[2] UKAEA, Culham Campus, Abingdon OX14 3DB, United Kingdom of Great Britain and Northern Ireland
[3] York Plasma Institute, University of York, Heslington, York YO10 5DQ, United Kingdom of Great Britain and Northern Ireland
[4] Max Planck Institute for Plasma Physics, 85748 Garching bei München, Germany

E-mail: J.Bryant@liverpool.ac.uk

Received 8 August 2024
Accepted for publication 7 February 2025
Published 18 February 2025

Abstract

Presently, SOLPS-ITER does not replicate the levels of plasma-molecular interactions seen during deep detachment on the Super-X divertors of MAST-Upgrade and TCV. At low temperatures ($T_e < 1$ eV) relevant to deep detachment, the AMJUEL reaction database contains discrepancies for detachment relevant molecular processes. In order to correct this the vibrationally resolved ground state Yacora model for H_2 (Yacora $H_2(X^1, v)$) has been used to calculate the vibrational distribution and thus from the cross-sections of the Yacora $H_2(X^1, v)$ model effective rate coefficients for these molecular processes. Reduced and extended implementations of Yacora $H_2(X^1, v)$ were constructed to form EIRENE-style databases for use in SOLPS-ITER. The reduced implementation utilises the same processes as EIRENE, but with updated cross-sectional data, whilst the extended implementation adds additional processes. The improved cross-sectional data lowers the threshold for molecular charge exchange (MCX) compared to AMJUEL, whilst the inclusion of the additional processes boosts the vibrational excitation in the molecular ground state providing the additional excitation energy required for MCX to be significant at low temperatures ($T_e < 5$ eV). When applied to a SOLPS-ITER isolated divertor leg setup, both implementations produce greater levels of MCX that result in elevated molecular ion densities (D_2^+) than the default rate setup. The higher levels of D_2^+ contribute to detachment via increased levels of Molecular Activated Recombination and Molecular Activated Dissociation. These plasma-molecular interactions elevate the neutral population. During detachment this has a strong impact on power and momentum losses, as well as elevated levels of Balmer α line emission and an earlier onset of the ion target flux rollover. These effects are strongest when the extended database is used.

* Author to whom any correspondence should be addressed.

Keywords: exhaust, plasma chemistry, detachment, alternative divertors, tokamak, scrape off layer

Some figures may appear in colour only in the online journal

1. Introduction

Future large, high power tokamaks, such as ITER, STEP, and EU-DEMO are predicted to deal with extreme target power loads that exceed the functional limit of the plasma-facing components that will be used on reactor class devices [1–3]. A functioning tokamak power plant will require detached divertors to greatly reduce the extreme parallel heat and particle fluxes predicted, to avoid thermal damage and erosion of plasma-facing components [3, 4].

Detachment occurs when the plasma temperature near the target drops to low levels ($T_e <\sim 5\,\mathrm{eV}$). Access to detachment can be achieved by increasing the upstream density through hydrogen fuelling or through radiative cooling via impurity injection (which typically dominate above $T_e = 5\,\mathrm{eV}$) [4, 5]. Total flux expansion causes an increase in the radiating volume and reduces the plasma temperature and target heat loads by spreading the heat over a larger area. This enhances the radiating region leading to greater cooling which further lowers the heat flux and plasma temperature over a region upstream of the target. As the hot, ionising plasma detaches from the target, neutrals accumulate downstream of the ionisation region, where processes such as volume recombination and plasma-neutral friction become dominant. This reduces the target particle (e.g. ion) flux through a collection of power, particle and momentum losses [6–8]. Below $T_e = 1\,\mathrm{eV}$, atomic volume recombination becomes significant which further increases the neutral density in the detached plasma [6, 7].

Atomic processes, such as electron-impact excitation (EIE) and electron–ion recombination (EIR) can result in significant hydrogen line emission and hydrogenic radiation. Power losses from EIE can lead to power limitation/starvation of the ion sources, whilst EIR can reduce the ion target flux by recombining the ions volumetrically. These direct atomic processes do not account for the all the hydrogenic line emission and reduction in the ion target flux seen during deep detachment on long-legged divertors with strong baffling on devices such as TCV and MAST Upgrade [9, 10]. The MAST Upgrade Super-X divertor combines increased neutral retention (atomic and molecular) with total flux expansion. This leads to further cooling of the divertor and the deepening of detachment via emissions from excited deuterium atoms *after plasma-molecular chemistry*. Compared to divertors on other devices, the MAST Upgrade Super-X has a relatively low divertor electron density ($n_e \approx 10^{19}\,\mathrm{m}^{-3}$) which leads to the appearance of the EIR peak at very low electron temperatures ($T_e << 0.5\,\mathrm{eV}$). Therefore, plasma-molecular interactions still play a key role in detachment until these extremely low temperatures in the Super-X configuration [9].

This plasma-molecular chemistry depends on the production of deuterium molecular ions (D_2^+) [11]. Interactions between these ions and the plasma can result in effective volumetric recombination of D^+ through Molecular Activated Recombination (MAR) lowering the ion target flux; additional means of dissociating molecules apart from electron-impact dissociation (EID) (Molecular Activated Dissociation—MAD); as well as additional sources of D^+ through Molecular Activated Ionisation (MAI). MAR and MAD result in excited deuterium atoms, which emit photons via de-excitation, resulting in radiative losses [10, 11]. The cooling of the internal temperature of these neutrals through de-excitation ultimately lowers the plasma temperature. Such interactions (particularly MAD and MAI) result in power losses to the electrons, both through radiative decay as well as through the threshold energy needed for dissociation and ionisation. To create these species in the sub 5 eV region left behind after detachment onset requires a high molecular density and vibrational excitation [11]. Highly vibrationally excited molecules increase the likelihood of molecular charge exchange (MCX) ($D^+ + D_2(v) \rightarrow D_2^+ + D$).

Numerical modelling is used to understand the exhaust region of fusion devices such as TCV and MAST Upgrade. This knowledge is then used to design future devices. SOLPS-ITER is the workhorse multifluid code which couples the B2.5 edge fluid solver and the EIRENE neutral Monte-Carlo solver [12]. B2.5 solves a set of equations based on the Braginskii fluid formulation, whilst EIRENE tracks neutral species for use in plasma-neutral interactions [13, 14]. EIRENE utilises the AMJUEL database for its atomic and molecular data needs. For deuterium plasma, SOLPS-ITER does not replicate the levels of MAR and MAD seen experimentally on MAST-U and TCV [9, 10, 15]. One possible discrepancy is the underestimation of the creation of D_2^+ in simulation which originates from MCX. The default AMJUEL MCX rate coefficient contains a severe decay below 1 eV when compared to newer, more detailed calculations [16–19]. When EIRENE mass-rescales these hydrogen-based rate coefficients to deuterium (the main ion species typically used in MAST Upgrade and TCV) this discrepancy is exacerbated, shifting the onset of this decay to 2 eV [11]. This work focuses on the utilisation of effective rate coefficients calculated with the Yacora $H_2(X^1, v)$ model as input for SOLPS-ITER [20]. Yacora $H_2(X^1, v)$ includes updated cross-sectional data for most molecular processes in AMJUEL, as well as reactions

not considered in the collisional radiative (CR) model, which has been used to calculate the AMJUEL database.

2. Numerical setup

2.1. CR modelling

In order to evaluate the population distribution of the vibrational states of molecular hydrogen needed to calculate effective rate coefficients, CR models are typically used. CR models evaluate a set of rate equations, balancing competing processes to predict population densities for excited states in atoms, molecules, and ions. Based on the notation from Greenland we write the evolution of state k using the following equation [21]

$$\frac{\mathrm{d}n_k}{\mathrm{d}t} = \sum_j A_j^k n_j - n_k \sum_j A_k^j + \sum_{i,j} R_{i,j}^k(T)\, n_i n_j - n_k \sum_{i,j} R_{i,k}^j(T)\, n_i + \Gamma_k \tag{1}$$

where n_k is the density of state k, A_j^k is the Einstein coefficient for spontaneous decay from $j \to k$, $R_{i,j}^k(T)$ is the production rate coefficient of state k from the collision of states i and j at temperature T, and Γ_k is the external source of species k. The production terms include recombination, excitation and spontaneous emission to the state being solved. The destructive terms will include reactions such as ionisation, de-excitation, and dissociation, to name a few. The external source term, Γ_k, can include three-body processes such as three-body recombination. All the reaction rates for the included states in the CR model form a coupled set of ordinary differential equations.

2.2. Yacora $H_2(X^1, v)$ CR model

Yacora is a tool created to evaluate CR models. A further detailed explanation for this solver can be found in Wünderlich *et al* [22]. The Yacora vibrationally resolved ground state model for H_2 (Yacora $H_2(X^1, v)$) was applied (with not all available reaction channels being activated) to calculate vibrational distributions, which have then been used to calculate effective rate coefficients. The inputted cross-sections were converted into rate coefficients by assuming a Maxwellian electron-energy distribution function. This model uses 15 vibrational levels below the dissociation limit in the electronic ground state of H_2 [20]. The Yacora $H_2(X^1, v)$ model includes collisional and spontaneous transitions to and from the 37 and 13 vibrational levels of the B^1 and C^1 singlet electronic states of H_2, respectively. The de-excitation reaction rate coefficients were evaluated using the principle of detailed balance [22–24]. A rotational ground state has been assumed and the rotational coupling to the vibrational and electronic distributions has been neglected [25]. Electronic transitions between excited electronic levels are neglected. In addition, the dissociation of the B^1 and C^1 singlet electronic states of H_2 was not included. This formulation does not have an attached hydrogenic atomic CR model and all generated atoms are assumed to be in the ground state. The reactions involved in the extended model are detailed in table 1 (section 2.3). A further detailed explanation of the extended model can be found in Bergmayr *et al* [20].

2.3. EIRENE-style databases

To assess the differences between the effect of updated cross-sections and additionally included reactions not present in the EIRENE vibrationally-resolved database (H2VIBR), a reduced implementation of Yacora $H_2(X^1, v)$ was created which featured the same reactions present in H2VIBR. This was used to form the X1RED database. This was appraised against the extended implementation of Yacora $H_2(X^1, v)$ model and which forms the X1EXT database. Table 1 compares the reactions involved in each database.

To calculate an effective molecular rate coefficient, the sum of the individual reaction rate coefficients for each vibrational level, originating from the Yacora $H_2(X^1, v)$ model, are weighted based on a calculated vibrational distribution. The following equation displays how an effective rate is calculated

$$< \sigma v >_{\mathrm{eff}} (T) = \sum_v f_v(T) < \sigma v >_v (T) \tag{2}$$

where $< \sigma v >_{\mathrm{eff}}$ is the effective reaction rate for a particular process of H_2, f_v is the vibrational distribution, and $< \sigma v >_v$ is the reaction rate vibrational level v [26]. It is assumed that $T = T_\mathrm{e} = T_\mathrm{i}$.

In order to calculate the vibrational distributions needed to form the effective rate coefficient databases, the Yacora $H_2(X^1, v)$ model was evaluated over the same conditions which were used to construct the AMJUEL database [27]. These conditions cover the temperature range of $T_\mathrm{e} = 0.1$–1000 eV and an electron density range of $n_\mathrm{e} = 1 \times 10^{14}$–$1 \times 10^{22}\,\mathrm{m}^{-3}$. Thus spanning a regime where coronal equilibrium applies (low densities), where a thermal equilibrium applies (high densities) and intermediate regimes where collisional-radiative modelling is required (intermediate densities) [21, 27]. Quasineutrality and a pure hydrogenic plasma ($Z_\mathrm{eff} = 1$) was assumed in these calculations, so $n_\mathrm{e} = n_\mathrm{i}$. For simplicity, $T_\mathrm{e} = T_\mathrm{i}$ is assumed. To calculate a vibrational distribution of the electronic ground state $H_2(X^1, v)$, the following species were set up as reservoir species ($H_2(v = 0)$,H_2^+,H,H^+,H^- and e^-). These species are an unlimited source of particles at fixed density and temperatures [21, 28, 29]. The other vibrational levels of the ground state were allowed to vary. Reservoir species in the Yacora $H_2(X^1, v)$ model are not independent of each other. $H_2(v = 0)$, was fixed to be 20%–50% of the n_e at the temperature of $T = 0.1$ eV to replicate the 'at rest' conditions in AMJUEL [27]. These molecular densities cover the different attached and detached regimes seen in experiment and simulation [28, 30–33]. H, H^-, and H_2^+ were given the H_2 Franck–Condon dissociation energy $T = 2.2$ eV (which arises from plasma-molecular reactions) and were fixed to densities seen in modelling associated with each electron density [28, 34–36].

Table 1. Comparison of processes included in EIRENE-style rate databases. * denotes reactions originating from the AMJUEL database that are not present in H2VIBR. The reference data for the X1RED and X1EXT databases can be found in Bergmayr *et al* [20].

Process	Reaction	H2VIBR/X1RED	X1EXT
Electron-impact-dissociation	$e + H_2(v) \rightarrow e + H + H$	✓	✓
Dissociative-attachment	$e + H_2(v) \rightarrow e + H + H^-$	✓	✓
Molecular-charge-exchange	$p + H_2(v) \rightarrow H + H_2^+$	✓	✓
Non-dissociative-ionisation	$e + H_2(v) \rightarrow e + e + H_2^+$	✓	✓
Dissociative-ionisation	$e + H_2(v) \rightarrow e + e + H + H^+$	✓*	✓
Electron-impact-excitation (neighbouring only)	$e + H_2(v) \rightarrow e + H_2(v \pm 1)$	✓	✓
Off-diagonal EIE	$e + H_2(v) \rightarrow e + H_2(v')$		✓
Radiative-recombination	$e + H_2^+ \rightarrow H_2(v') + \gamma$		✓
3-body-recombination	$e + e + H_2^+ \rightarrow e + H_2(v')$		✓
Electron-impact-excitation B^1/C^1	$e + H_2(v) \rightarrow e + H_2(B^1/C^1, v')$ $e + H_2(B^1/C^1, v) \rightarrow e + H_2(v')$		✓
Spontaneous-emission B^1/C^1	$H_2(B^1/C^1, v) \rightarrow H_2(v') + \gamma$		✓

Once a vibrational distribution has been evaluated for each density point, effective rate coefficients for all reactions in the CR model can be formed. To construct an EIRENE-style database, these effective rate coefficients must be fitted to a polynomial with both temperature and density dependent terms (H.4 fit). Below the evaluated density limit (coronal regime), the polynomial fit asymptotically collapses to a fit dependent only on temperature. In addition to the double polynomial fits, at this density single polynomial temperature fits were also created (H.2 fit) [27]. The individual rate coefficients for each vibrational level are included in each database as single polynomial temperature fits. Figure 1 details the normalised vibrational distribution for cases of the Yacora $H_2(X^1, v)$ model using rate coefficients from H2VIBR (and the dissociative ionisation rate H.4 2.2.10 from AMJUEL), the updated cross-sections for the same reactions (X1RED), and the extended implementation of the Yacora $H_2(X^1, v)$ model (X1EXT). These reactions are detailed in table 1.

Figure 1 shows an increase of high vibrational levels at high T_e for the X1EXT database when compared to the H2VIBR database. X1EXT considers excitation to the B^1 and C^1 singlet electronic states of H_2 and includes vibrationally resolved radiative decay into the ground state. The inclusion of off-diagonal vibrational transitions and the vibrational redistribution via these electronically excited states results in a boosting of vibrational excitation in the ground state. Below the detachment temperature threshold $T_e = 5\,\text{eV}$, the higher vibrational level population provides the additional excitation energy needed for MCX to be significant between $1 < T_e < 5\,\text{eV}$ [11]. Above $T_e = 5\,\text{eV}$ it is assumed that ionisation dominates and molecular densities are low, thus limiting plasma-molecular interactions. For all cases, the population of the higher vibrational levels decreases below $T_e = 0.5\,\text{eV}$, this correlates with the onset in the decay of the MCX effective rate coefficient seen in figure 3. At this temperature EIR begins to compete with MAR as the dominant recombination process on the MAST Upgrade Super-X.

3. Effective rate results

3.1. Effective rate comparison

This section focuses on the application of the effective rate coefficients calculated using the vibrational distribution and cross-sectional data from the Yacora $H_2(X^1, v)$ model to zero-dimensional analysis. The key reactions that this study will investigate are MCX, non-dissociative ionisation (NDI), and EID as they contribute to plasma-molecular interactions that increase the atomic neutral population, ultimately deepening detachment through additional radiative cooling and increasing the density of the neutral cloud ahead of the target.

Large differences between AMJUEL and the X1RED/X1EXT databases, arise from the vibrationally-resolved rate coefficients used in the effective rate coefficient calculations. Many of the AMJUEL calculations are based on analytic scalings that assume a temperature-independent, constant, difference between the interaction rates of different vibrational levels. For instance, the H2VIBR MCX rate coefficients assume that $< \sigma v >_{\text{MCX},v} (T) = A_v < \sigma v >_{\text{MCX},v=0} (T)$, where A_v is a scaling factor from Greenland [37]. This is illustrated in figure 2.

Figure 2 shows that all the H2VIBR rate coefficients decay at $T < 1\,\text{eV}$ as this occurs for $< \sigma v >_{\text{MCX},v=0} (T)$. Therefore, the AMJUEL MCX effective rate coefficient which was calculated using these scaled vibrationally-resolved rate coefficients and a vibrational distribution from H2VIBR contains this decay. In contrast, this sharp decay does not occur for $v \geq 4$ when more detailed calculations for MCX are used, as those employed in the Yacora $H_2(X^1, v)$ model [17–19] as well as *abinitio* vibrationally resolved calculations [16].

As mentioned previously, the key differences between the models that form the X1EXT and X1RED databases is the inclusion of off-diagonal electron-impact-excitation within the electronic ground state as well as the excitation to the B^1

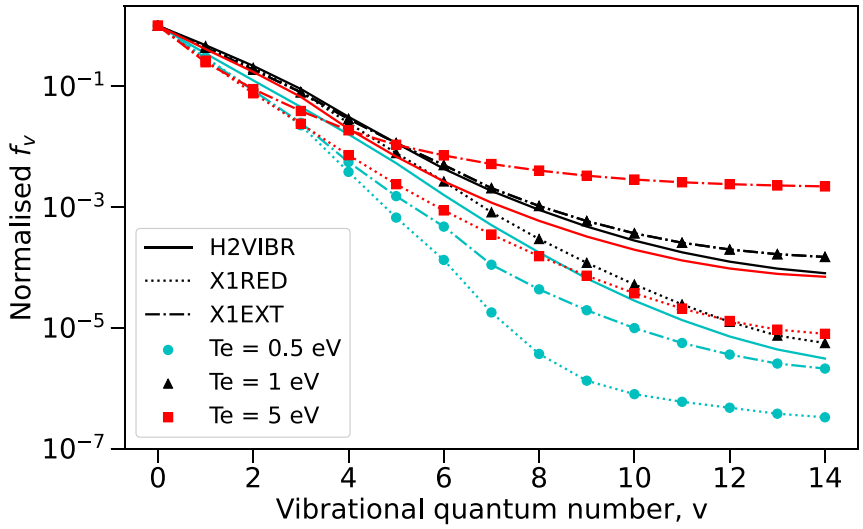

Figure 1. Vibrational population densities relative to the $H_2(v=0)$ density at the plasma density $n_e = 1 \times 10^{19} m^{-3}$ predicted by the reduced (X1RED) and extended (X1EXT) implementations of the Yacora $H_2(X^1, v)$ model superimposed on the corresponding H2VIBR predictions at fixed plasma temperatures.

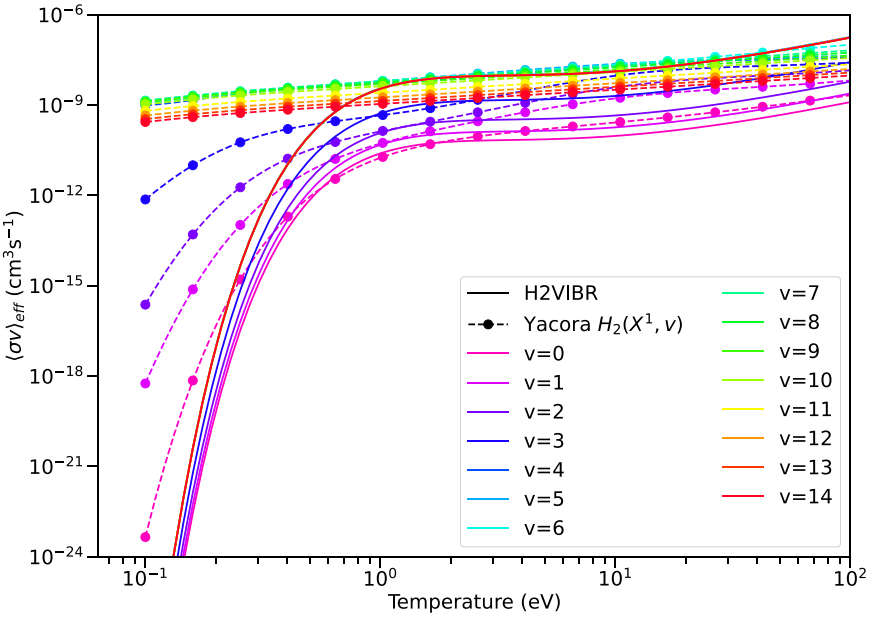

Figure 2. Vibrationally-resolved molecular charge exchange rate coefficients from H2VIBR (solid) and the Yacora $H_2(X^1, v)$ model (dashed) denoted for each vibrational level of the molecular ground state.

and C^1 electronic states followed by radiative decay into the ground state. These reactions populate the higher vibrational levels at low temperatures. This provides the excitation energy needed to lower the requirements for MCX. At $T_e = 0.25\,eV$ this leads to a factor of ~ 100 difference between the two effective rate coefficients which is shown in figure 3.

The EID and NDI effective rate coefficients in AMJUEL were calculated in an analogous manner to MCX. The $< \sigma v >_{v=0}$ is still provided by Janev which is then scaled using the Greenland formulation to form an effective rate coefficient [37, 38]. However, the Sawada CR model was used to provide the assumed vibrational distribution via the following equation

$$< \sigma v >_{\text{eff}} (T_e) = \sum_v f_v (T_e) A_v < \sigma v >_{v=0} (T_e, n_e) . \quad (3)$$

The Sawada CR model assumes a vibrational ground state and a single summed vibrational excited state. An electron density dependence is introduced into $< \sigma v >_{v=0}$ (and hence the AMJUEL EID and NDI effective rate coefficients) through the consideration of electronically excited levels of both H_2 and H in the Sawada CR model [26]. This method neglects

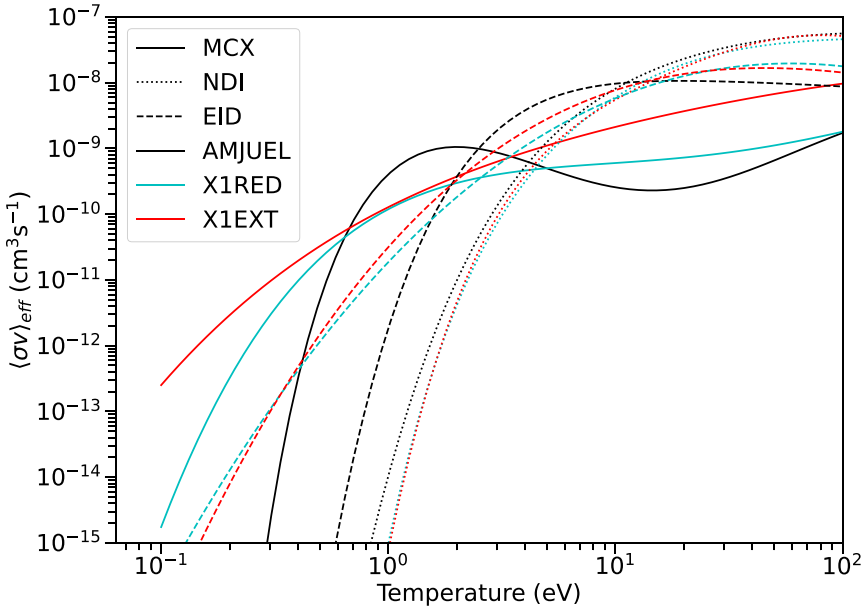

Figure 3. Effective reaction rate coefficient comparison for molecular charge exchange (MCX), non-dissociative ionisation (NDI), and electron-impact dissociation (EID). The AMJUEL MCX, NDI, and EID rate coefficient fits used were H.2 3.2.3, H.4 2.2.9, and H.4 2.2.5g respectively. X1RED used temperature dependent fits. All X1EXT reaction rate coefficient fits used were density and temperature dependent. The density and temperature dependent polynomial fits used were evaluated at $n_e = 1 \times 10^{19}\,m^{-3}$.

Table 2. Relative errors in the polynomial fitting of the effective rate coefficients for the AMJUEL, X1RED, and X1EXT databases. The method of error propagation originates from Janev *et al* and was used in the AMJUEL database [27, 38].

	Maximum relative error (%)		
Reaction	AMJUEL	X1RED	X1EXT
Molecular charge exchange	10.20	13.92	8.26
Non-dissociative ionisation	3.10	0.91	3.20
Electron-impact dissociation	11.64	15.05	6.58

the reduction in the threshold energy for EID at higher vibrational levels, which is included by the *abinitio* MCCC calculations used by the Yacora $H_2(X^1, v)$ model [39]. This is present but not as impactful in NDI since the threshold energies are relatively similar for all vibrational levels in the ground state.

Therefore, the calculated X1RED effective rate coefficients will not have an electron density dependence, since the interactions involved in obtaining the electronic ground state vibrational distribution are all linearly dependent on electron density and multi-step processes are not included. Conversely, all X1EXT effective rate coefficients calculated contain an electron density dependence. X1EXT includes collisional (de-)excitation and radiative decay from the electronic ground state to the singlet states of H_2 (B^1, C^1) and H_2^+, as well as two and three-body recombination of H_2^+, which introduce an electron density dependence in the vibrational distribution of the ground state. In this case, it should be noted that the electron density dependence of the effective rate only enters through the electron density dependence of the vibrational distribution of the ground state, f_v. In comparison, the inclusion of the electronic excited states of H_2 and H in the Sawada CR model used to calculate EID and NDI in AMJUEL contains a stronger electron density dependence than present in X1EXT. Figure 3 details the effective rate coefficients explored in this paper.

The X1RED and X1EXT MCX and EID rate coefficients show a marked increase at low temperatures relevant to detachment and should increase the levels of MAR, MAD, and dissociation of H_2 in simulation. The AMJUEL MCX rate coefficient begins to decay at $T_e = 1\,eV$ and the X1RED and X1EXT are relevant below $T_e = 0.5\,eV$. Below $T_e = 1\,eV$ the X1RED and X1EXT rate coefficients are still relevant. The NDI rate coefficients are similar but at this density are slightly higher in the AMJUEL case compared with the X1RED and X1EXT cases. The relative errors in the polynomial fitting of these rate coefficients compared to their effective rate coefficient calculations are presented in table 2.

The maximum relative errors for the NDI effective rate coefficients are similar for all three databases, but is lowest in the X1RED database due to the fitting being only electron temperature dependent. Therefore, the error was calculated for 9 polynomials coefficients instead of the 81 polynomial coefficients for electron temperature and density dependent fits. The X1EXT database has lower maximum relative errors than AMJUEL for MCX and EID. The maximum relative error in the X1RED fits for these reactions are higher than AMJUEL

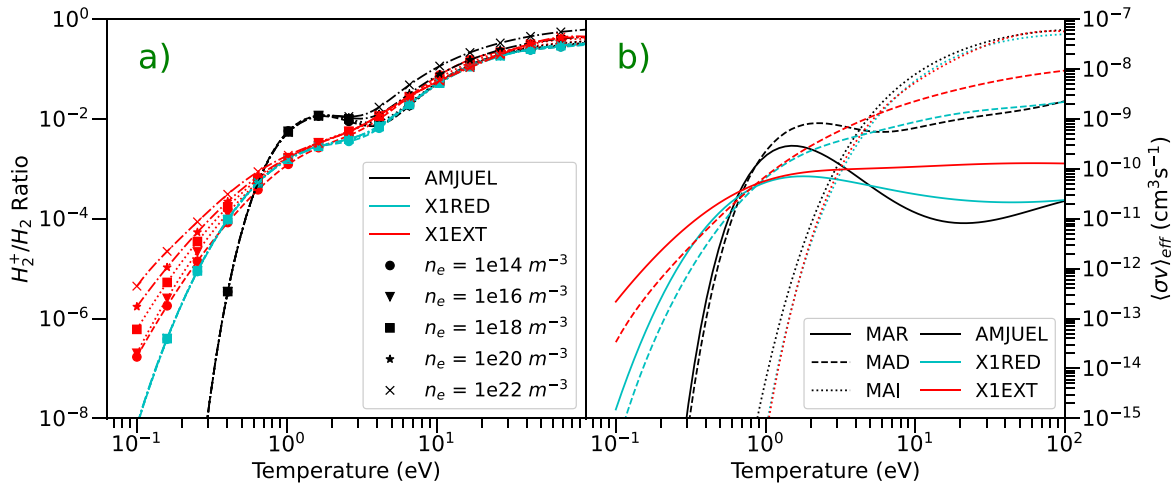

Figure 4. (*a*) Production ratio of H_2^+ at various electron densities for the AMJUEL (black), X1RED (cyan), and X1EXT (red) databases. (*b*) Plasma-molecular interactions evaluated at $n_e = 1 \times 10^{19}\,m^{-3}$ for the AMJUEL, X1RED, and X1EXT databases.

due to the decay in the vibrational distribution at low temperatures ($T_e < 1\,eV$) for that model as seen in figure 1. Overall, the X1EXT fits are relatively more accurate than AMJUEL for these reactions.

The increase in MCX results in an increase in H_2^+ content, which is approximated by equation (4) as the ratio of H_2^+ creation over its destruction, assuming H_2^+ is instantaneously created and destroyed—ignoring transport effects (as is assumed by EIRENE)

$$\frac{nH_2^+}{nH_2} = \frac{\left(< \sigma v >_{\text{eff}}^{H_2,\text{MCX}} + < \sigma v >_{\text{eff}}^{H_2,\text{Ion}}\right)}{\left(< \sigma v >_{\text{eff}}^{H_2^+,\text{DR}} + < \sigma v >_{\text{eff}}^{H_2^+,\text{DI}} + < \sigma v >_{\text{eff}}^{H_2^+,\text{DE}}\right)}. \tag{4}$$

The creation term is the sum of the effective MCX and ionisation. The destructive term is the sum of the effective dissociative recombination (DR), ionisation (DI), and excitation (DE) of H_2^+ into other species. The destructive reaction rate coefficients used are from the AMJUEL database (reactions H.4 2.2.14, H.4 2.2.11, and H.4 2.2.12, respectively). The produced H_2^+ then undergoes dissociative recombination ($e + H_2^+ \rightarrow H + H$) for MAR, undergoes dissociative excitation ($e + H_2^+ \rightarrow e + H + H^+$) for MAD, and undergoes dissociative ionisation ($e + H_2^+ \rightarrow 2e + 2H^+$) for MAI. Figure 4 demonstrates the differences in the production of H_2^+ for each model, in addition to the zero-dimensional evaluation of MAR, MAD, and MAI at $n_e = 1 \times 10^{19}\,m^{-3}$.

The production of H_2^+ is higher at lower temperatures in the X1EXT and X1RED cases than the AMJUEL case. Below 0.5 eV X1EXT gives the highest result of all three investigated databases. Cross-sectional differences between the MCX effective rate coefficients lead to an increase in H_2^+ from the AMJUEL case for $0.5 < T_e < 3\,eV$. In the $n_e = 1 \times 10^{22}\,m^{-3}$ evaluation, the extended model produces approximately 100 × more H_2^+ than the $n_e = 1 \times 10^{14}\,m^{-3}$ evaluation at temperatures below 0.3 eV. The electron density dependence present in the AMJUEL NDI effective rate coefficient (originating from the inclusion of excited electronic states of H and H_2) leads to greater production of H_2^+ at higher densities when compared to the X1RED and X1EXT databases. The increased vibrational excitation for X1EXT at low temperatures originates from the inclusion of off-diagonal electron-impact-excitation compared to AMJUEL and X1RED. At high density, the increased collisionality leads to a greater excitation to the electronic states followed by the decay into the higher vibrationally excited levels of the ground state, further lowering the requirements for MCX.

Figure 4 shows that the levels of MAI are similar for all three databases. However, MAR and MAD are significantly higher below $T_e = 0.5\,eV$ and above 3 eV for both X1RED and X1EXT databases when compared to AMJUEL. The levels of MAR and MAD in the X1EXT are notably stronger than that of the X1RED rate coefficients. The AMJUEL rate model predicts a steep decline in the levels of plasma-molecular interactions below $T_e = 1\,eV$, this does not agree with the inference from MAST Upgrade Super-X experiments, which suggests that these interactions are still relevant at very low temperatures [9]. Both the X1RED and X1EXT databases provide better agreement with this trend.

When applied to simulation EIRENE rescales these hydrogen based reactions to the main ion species (i.e. deuterium in TCV and MAST-U). This exacerbates the decay in the MCX effective rate coefficient and hence MAR and MAD. For ion-impact collisions, such as MCX, EIRENE rescales the effective rate coefficients by dividing the plasma temperature by the mass number to ensure the impacting ion has the correct velocity for the same ion temperature. Thus maintaining the correct collisionality for these reactions. This is incorrect as EIRENE also scales the electron temperature dependent vibrational distribution included in the effective molecular rate coefficients in addition to the cross-sectional data [11]. This can be seen in the following equation

$$< \sigma v >_{D_2,\text{eff}} (T_e) = \sum_v f_v (T_e/2) < \sigma v >_{H_2,v} (T_i/2). \tag{5}$$

Further details on the EIRENE mass-rescaling can be found in [35]. Additionally, it is assumed that no isotopical differences exist in the reaction rate coefficients and neither in the energy levels of the vibrational distribution between the different isotopes, which is incorrect [40]. Molecular charge exchange is the only mass-rescaled reaction in this paper. Figure 5 displays the effect of this mass-rescaling.

This mass-rescaling shifts the decay in the AMJUEL MCX effective rate coefficient to begin at 2 eV, and exacerbates the decay in X1RED and X1EXT [11]. Thus decreasing the strength of MAR and MAD below 1 eV for X1RED and X1EXT. The difference between the rate coefficients is a conservative estimate, as the, *incorrectly*, applied ion isotope mass-rescaling reduces the X1RED/X1EXT MCX effective rate coefficient more than that of H2VIBR/AMJUEL, since they are more sensitive to the temperature dependency of the vibrational distribution. The X1EXT and X1RED databases improve on the molecular rate coefficients in AMJUEL but, since they are derived for hydrogen, are still affected by these two shortcomings when applied in SOLPS-ITER to deuterium and tritium simulations [11].

4. SOLPS-ITER simulation results

4.1. SOLPS-ITER simulation setup

In the interest of highlighting the differences between the respective rate models in SOLPS-ITER, an isolated divertor leg geometry is used. This geometry originates from Moulton *et al* [41]. The grid is shown in figure 6. This geometry fixes upstream conditions, ensures neutral closure, and limits cross-field transport, which is ideal to isolate the effect of the different models on detachment (in the absence of drifts, currents, and impurities).

In figure 6, Z and R are the vertical and major radius coordinates respectively. Typical MAST Upgrade magnetic field values are used. In the poloidal direction, the field is given by $B_x = \alpha_x/R$ where $\alpha_x = 0.025\,\mathrm{Tm}$. The toroidal field is given by $B_z = \alpha_z/R$ where $\alpha_z = 0.5\,\mathrm{Tm}$. This sets the total flux expansion over this grid to be $f_R = R_t/R_u = 1.64$. The transport coefficients were set to $D_y^n = \chi_y^e = \chi_y^i = 1\,\mathrm{m^2 s^{-1}}$, and the density and heat flux decay lengths were set to $\lambda_n = 10\,\mathrm{cm}$ and $\lambda_q = 5\,\mathrm{cm}$, respectively [41]. Deuterium was used in the SOLPS-ITER simulations, thus the two shortcomings in the isotope dependencies mentioned above apply.

Carbon is the wall material used for all surfaces. The TRIM reflection model was used for deuterium on carbon [42]. The recycling percentage of ions and neutrals at the target was set to 99.9%, the remainder are absorbed by the walls. For all atomic and ionic species the reflection model is split into fast and thermal particle reflection components. This is dependent on the incident energy of each particle, E_{in}. In the incident energy range of $1 < E_{\mathrm{in}} < 50\,\mathrm{eV}$, 10% of these particles are thermally released from the walls as D_2 at the wall temperature, $T_{\mathrm{wall}} = 300\,\mathrm{K}$. Otherwise, these species are assumed to be fast particles and are recycled as D. Below this energy range, the thermal model is assumed and these species are reflected as D_2. Above this range the fast particle model is used. The reflection of molecules is always assumed to follow the thermal particle model [14]. At the bottom right of the grid, a pumping surface was placed. Its pumping fraction was set to $F_{\mathrm{pump}} = 0.05$. Although TRIM was used to compute the recycling from a carbon surface, no carbon sputtering was accounted for thus all effects are restricted to hydrogenic species.

With the aim of acquiring a full picture of the effect of the rate coefficient databases on the onset of detachment, a scan in upstream density for the SOLPS-ITER simulations over the following range of upstream densities $n_{\mathrm{e,u}} = 3 \times 10^{18}$–$9.6 \times 10^{18}\,\mathrm{m^{-3}}$ was performed. This covers a range of attached and detached cases. At the divertor entrance, the parallel heat flux density was set to $q_{||} = 20\,\mathrm{MWm^{-2}}$ to replicate MAST-U Ohmic L-mode parameters [15]. The reaction set used in the reference (AMJUEL) vibrationally-unresolved simulation setup is displayed in table 3.

For simulations featuring the X1RED and X1EXT databases the standard EIRENE input was used (as seen in table 3) but the input from AMJUEL was replaced with the respective effective rate coefficients of molecular-charge-exchange (MCX), electron-impact-dissociation (EID), and non-dissociative-ionisation (NDI) from X1RED or X1EXT. As previously mentioned, the X1RED polynomial fits were only electron temperature dependent, whilst the X1EXT polynomial fits are dependent on electron temperature and density.

4.2. Evolution of detachment

The subsequent section will focus on the effect of the different molecular rate coefficients on the evolution of the plasma parameters during a density scan. Figure 7 shows the ion target flux as function of the upstream density for each molecular rate model, together with the ion sources and sinks. As the upstream density is increased, the ion target flux first rises—reminiscent of the attached phase and, at higher upstream densities, flattens and rolls-over—typically considered the onset of detachment [43].

Comparing the ion target flux evolution between the X1EXT, X1RED and AMJUEL cases shows a relative 16% and 9% reduction in the roll-over (detachment onset) for the X1EXT and X1RED cases when compared to AMJUEL. Stronger reductions of the ion target flux occur in the X1EXT and X1RED cases, indicating deeper levels of detachment. The reduced detachment onset is facilitated by increased levels of MAR, which starts to occur near the ion target flux roll-over at moderate electron densities ($n_{\mathrm{e,u}} = 6 \times 10^{18}\,\mathrm{m^{-3}}$). The onset of MAR occurs when target electron temperatures of below 5 eV are reached. In contrast, EIR occurs when electron temperatures of sub 0.5 eV are reached. This occurs at the highest upstream densities $n_{\mathrm{e,u}} = 8 \times 10^{18}\,\mathrm{m^{-3}}$ for the X1EXT case, and $n_{\mathrm{e,u}} = 8.5 \times 10^{18}\,\mathrm{m^{-3}}$ for the X1RED and AMJUEL cases. This explains the much later roll-over in the AMJUEL case, where MAR is negligible. Stronger levels of EIR occur in the X1EXT case, further reducing the ion target flux. The rollover in target electron density occurs approximately two cases after the rollover in ion target flux for each case.

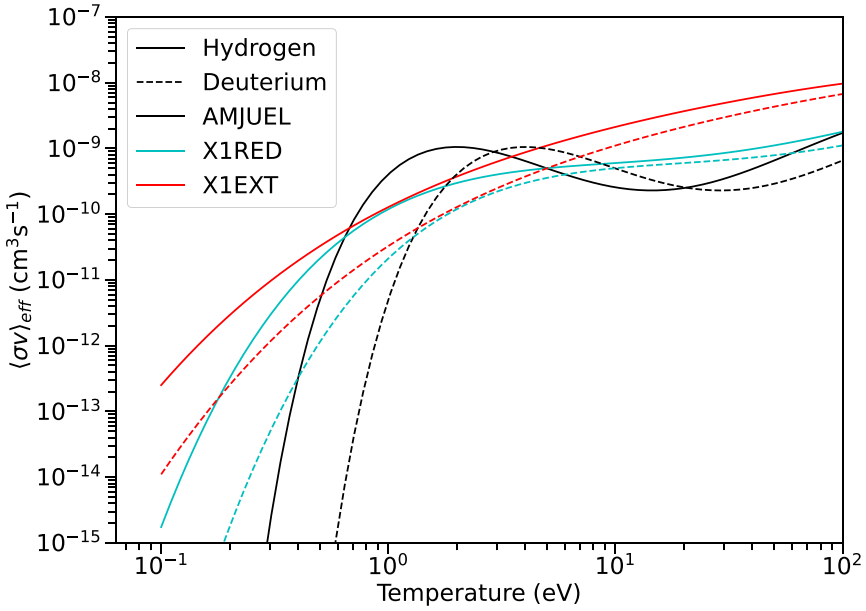

Figure 5. Comparison of the hydrogen (solid) based molecular charge exchange effective rate coefficient and the respective deuterium (dashed) mass-rescaled effective rate coefficient for each database: AMJUEL (black), X1RED (cyan) and X1EXT (red). The X1EXT effective rate coefficient is density and temperature dependent and was evaluated at $n_e = 1 \times 10^{19}\,m^{-3}$.

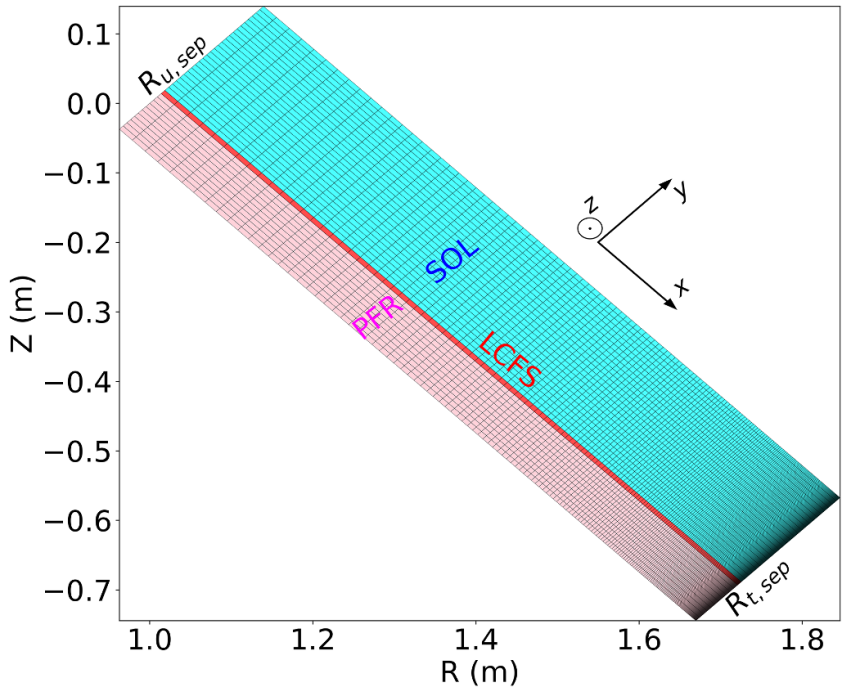

Figure 6. Isolated divertor leg SOLPS-ITER grid rotated 45 degrees from the X-point. The highlighted sections indicate different edge regions: (cyan)—the scrape-off-layer (SOL); (pink)—the private-flux-region (PFR); (red)—the last-closed-flux-surface (LCFS).

The target electron temperature is lower for the X1RED and X1EXT cases than the AMJUEL simulations at the highest electron densities, with X1EXT featuring the largest temperature drop. This drives the increase of EIR at the highest upstream densities for the X1EXT case, despite the target electron density being slightly reduced, compared to the AMJUEL case. These lower target temperatures are likely driven by the additional power losses associated with MAR and MAD. The lower plasma temperatures result in lower neutral temperatures, negating the increase in neutral density and resulting in similar neutral pressures for all three cases. It is worth noting that the X1RED and X1EXT cases roll-over at a target temperature of $T_e = 0.47\,eV$, whilst the AMJUEL case rolls-over at $T_e = 0.31\,eV$. The values for the X1RED and X1EXT cases are not too dissimilar to the those in Moulton *et al* which predicts values around $T_e = 0.53\,eV$ [41]. Such values are relative

Table 3. EIRENE reactions included in reference vibrationally-unresolved case. *B* denotes BGK approximated background species, used in neutral–neutral collisional processes [14].* denotes the reactions altered to the X1RED and X1EXT equivalent in each respective case.

Process	Reaction	Database code
Molecular-charge-exchange*	$D^+ + D_2 \rightarrow D + D_2^+$	AMJUEL H.2 3.2.3
Electron-impact-dissociation*	$e + D_2 \rightarrow e + 2D$	AMJUEL H.4 2.2.5g
Non-dissociative-ionisation*	$e + D_2 \rightarrow 2e + D_2^+$	AMJUEL H.4 2.2.9
Dissociative-ionisation	$e + D_2 \rightarrow 2e + D^+ + D$	AMJUEL H.4 2.2.10
D_2^+-dissociative-ionisation	$e + D_2^+ \rightarrow 2e + 2D^+$	AMJUEL H.4 2.2.11
D_2^+-dissociative-excitation	$e + D_2^+ \rightarrow e + D + D^+$	AMJUEL H.4 2.2.12
D_2^+-dissociative-recombination	$e + D_2^+ \rightarrow 2D$	AMJUEL H.4,8 2.2.14
Proton-molecule-collision	$D^+ + D_2 \rightarrow D_2 + D^+$	AMJUEL H.0,1,3 0.3T
Atomic-charge-exchange	$D^+ + D \rightarrow D + D^+$	HYDHEL H.1,3 3.1.8
Electron-impact-ionisation	$e + D \rightarrow 2e + D^+$	AMJUEL H.4,10 2.1.5
Electron–ion-recombination	$e + D^+ \rightarrow 2D$	AMJUEL H.4,10 2.1.8
Atom–atom-collision	$D + D(B) \rightarrow D + D(B)$	AMMONX H.2 R-H-H
Atom–molecule-collision	$D + D_2(B) \rightarrow D + D_2(B)$	AMMONX H.2 R-H-H2
Molecule–atom-collision	$D(B) + D_2 \rightarrow D(B) + D_2$	AMMONX H.2 R-H2-H
Molecule–molecule-collision	$D_2(B) + D_2 \rightarrow D_2(B) + D_2$	AMMONX H.2 R-H2-H2

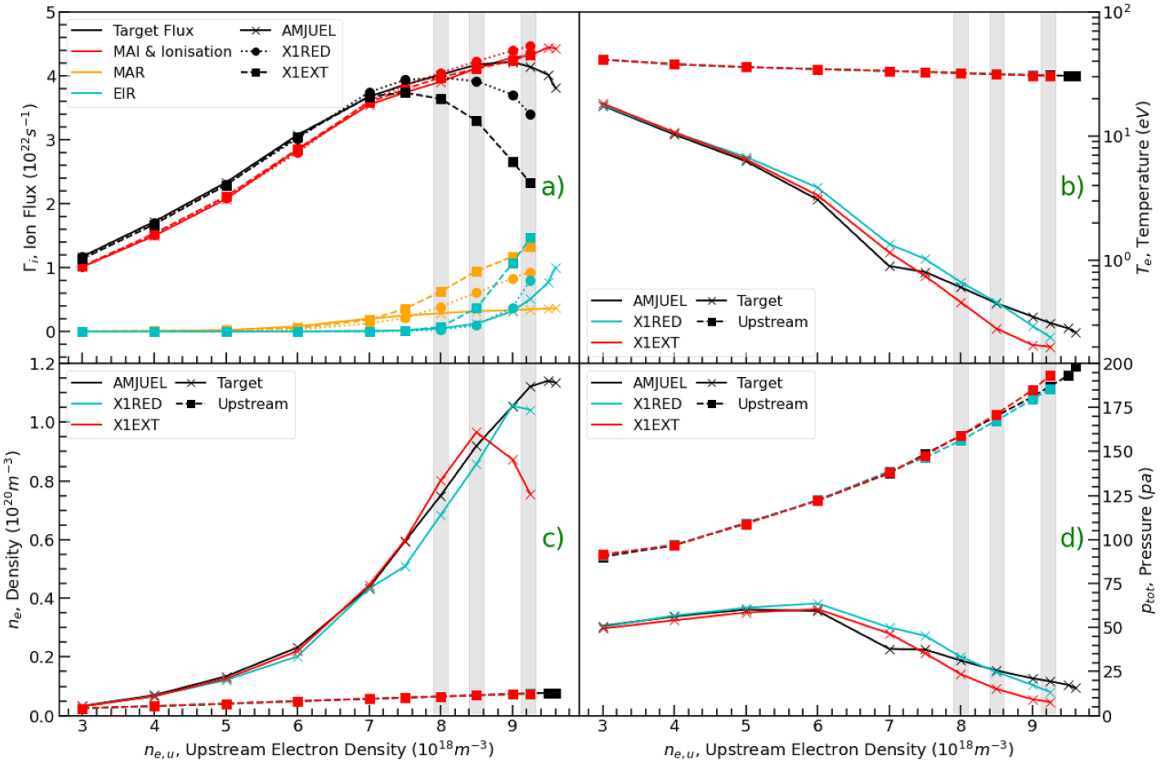

Figure 7. General plasma parameters over the upstream density range $n_{e,u} = 3 \times 10^{18} - 9.6 \times 10^{18}\,m^{-3}$ for the AMJUEL, X1RED, and X1EXT SOLPS-ITER implementations. (*a*) The integrated ion target flux (black) in addition to the integrated ion flux source of MAI & ionisation (red), as well as the integrated ion flux sinks of EIR (cyan) and MAR (orange); (*b*) electron upstream and target temperature; (*c*) electron upstream and target density; (*d*) total upstream and target pressure. This consists of static and dynamic pressure. The grey shaded areas indicate where ion target flux rollover occurs in each case.

since the number of simulations is limited. Key differences between the setups result in this lower rollover electron target temperature. These include BGK neutral–neutral elastic collisions (reducing plasma-molecular momentum losses via D_2 thermalisation with the walls and D), different recycling and pumping coefficients which are known to cause sensitivity in the target density, as well as target differences (Γ_i and T_e) by the use of the SOLPS-ITER code package instead of SOLPS5.0 [12, 41, 44–46].

The plasma target pressure drops significantly for all three cases before the ion target flux roll-over at $n_{e,u} = 7 \times 10^{18}\,m^{-3}$. The strongest target pressure reduction at the highest upstream densities occurs for the X1EXT case. This originates from the combination of the reduced plasma density

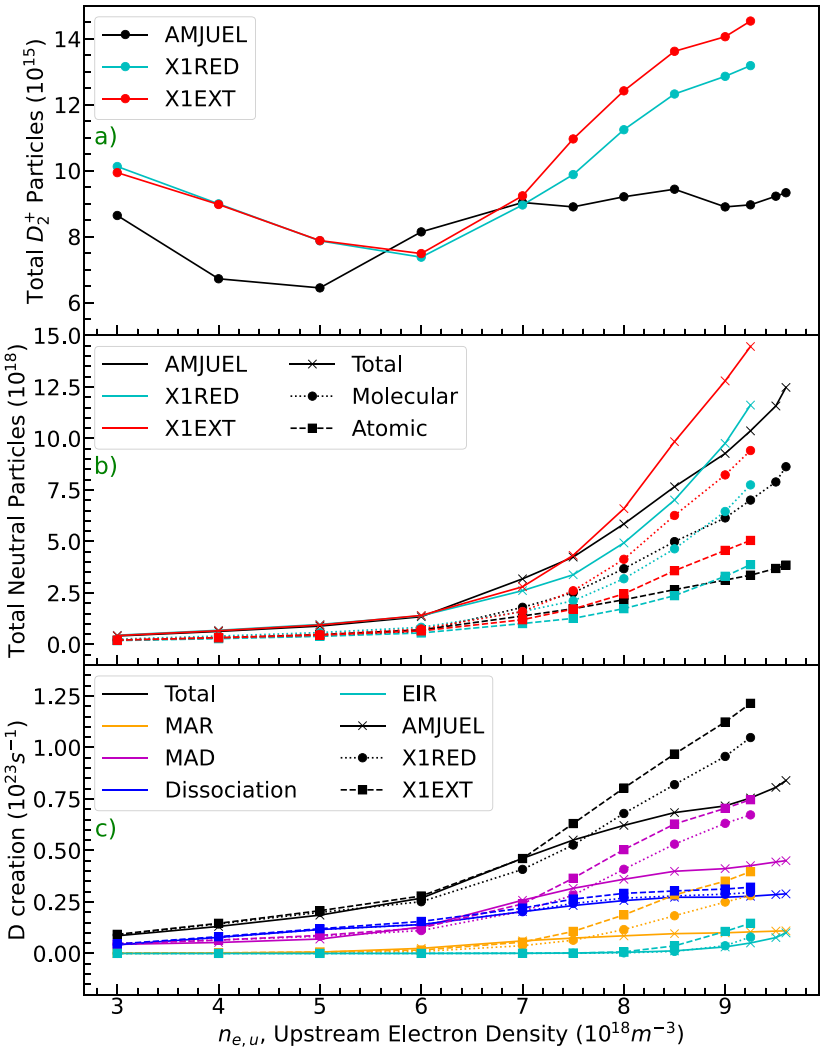

Figure 8. Relevant total species population and the volumetric production of D atoms for the AMJUEL, X1RED, and X1EXT SOLPS-ITER implementations over the upstream density range $n_{\mathrm{e,u}} = 3 \times 10^{18} - 9.6 \times 10^{18}\,\mathrm{m}^{-3}$. (*a*) Total neutral population (solid line), total molecular population (dotted line), and the total atomic population (dashed line); (*b*) total D_2^+ population; (*c*) post-processed volumetric n_D production source using the respective rate setups, from MAR (orange), MAD (magenta), EID (blue) and EIR (cyan). This method comes from Verhaegh *et al* [11].

due to the increased MAR and EIR and the reduction in target electron temperature. Upstream conditions, cross-field transport, and radial sources remain similar for all cases. The X1RED and X1EXT cases above $n_{\mathrm{e,u}} = 9.25 \times 10^{18}\,\mathrm{m}^{-3}$ struggled with convergence due numerical instabilities when the target electron temperatures dropped below $T_{\mathrm{e}} = 0.1\,\mathrm{eV}$.

Figure 8 shows that the molecular rate coefficients used in SOLPS-ITER have an important impact on the neutral atom and D_2^+ populations in the divertor. The D_2^+ population in the X1RED and X1EXT cases is much higher than the reference case, due to the increased MCX rate at low temperatures during detachment. This results in heightened MAD, increasing the volumetric deuterium atom source and thus the deuterium atom density. Figure 8 shows the total atomic creation rate has increased by around 50% from the AMJUEL to the X1EXT case, and by around 30% from the AMJUEL to the X1RED case at high density ($n_{\mathrm{e,u}} = 9.25 \times 10^{18}\,\mathrm{m}^{-3}$). EID is the most dominant source in the attached phase in all cases and is significant after detachment and, already prior to the detachment rollover in the X1RED and X1EXT cases, MAD and MAR become a pronounced source of neutral D creation. As detachment progresses, MAR and MAD become more pronounced, further increasing the neutral atom source. MAD cools the divertor lowering the plasma temperature below $T_{\mathrm{e}} = 0.5\,\mathrm{eV}$ where EIR becomes an additional source of neutrals and cooling. This increase in the atomic population results in heightened recycling into D_2. Hence, X1EXT has the most elevated molecular population.

4.3. Power losses

Target wall-loading is predominantly driven by the parallel plasma heat flux density, whereas neutral and photon heat loads are generally small. The parallel heat flux density, $q_{||}$, combines the particle flux, and plasma thermal energy whilst accounting for the ionisation energy released

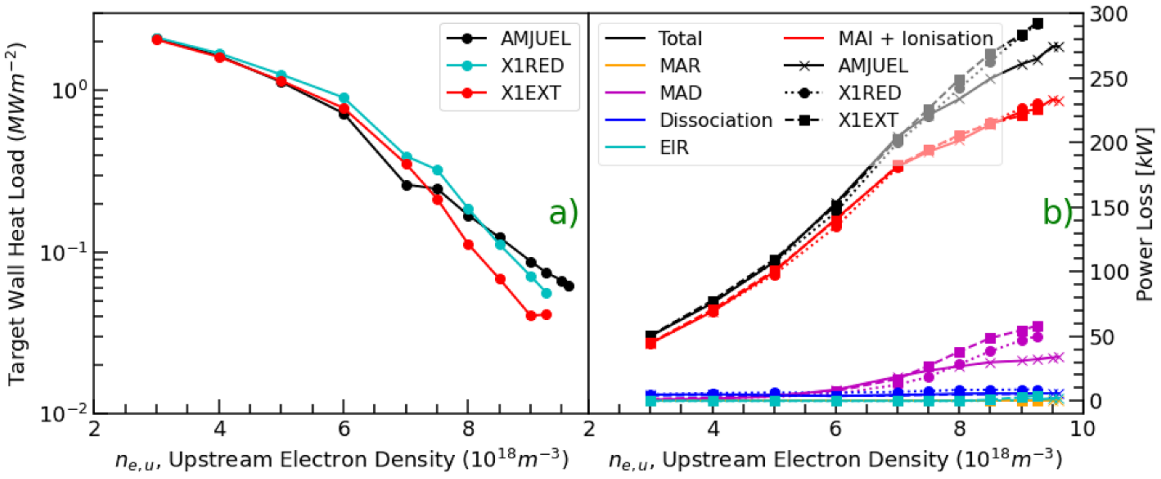

Figure 9. Impact of molecular effective rate coefficients on wall-loading and hydrogenic power losses. (*a*) Target wall heat load density for the AMJUEL, X1RED, and X1EXT models over the upstream density range $n_{e,u} = 3 \times 10^{18}$–$9.6 \times 10^{18}\,m^{-3}$. This consists of the target plasma and neutral loads. (*b*) Hydrogenic power losses evaluated over the entire isolated leg with each reaction as a function of upstream density for the AMJUEL, X1RED, and X1EXT SOLPS-ITER implementations. Post-processed using the respective rate setups, utilising the method from Verhaegh *et al* [11].

from surface recombination at the target [47, 48]. The neutrals impart thermal energy through collisions with the wall. Figure 9 shows the target power wall-loading for each database implementation.

The target wall heat load density (MWm^{-2}) drops considerably after detachment rollover in the X1RED and X1EXT cases compared to the AMJUEL reference case. The largest reduction in target wall heat load density being strongest in the X1EXT case. This appears to align with the reduction in target electron temperature seen in figure 7. This reduction in target electron temperature is linked with Power losses associated with ionisation, MAI, EID, and EIR are similar for all cases. However, power losses associated with MAD significantly increase from the AMJUEL to the X1RED and X1EXT cases and double during deep detachment. This culminates in the total power lost in the $n_{e,u} = 9.25 \times 10^{18}\,m^{-3}$ simulations being approximately 8% greater in the X1RED and X1EXT setups when compared to the AMJUEL case. The power losses associated with MAR are negligible, as the potential energy gained from the recombination process is radiated by the excited atoms, however the reduction in ion target flux provides a colder region where EIR can occur [11].

Photon-emission-coefficients (PECs) from Yacora (on the web) were used to estimate the Balmer alpha contributions from D, D_2, and D_2^+. Further details on the Yacora (on the web) PECs can be found in Verhaegh *et al* [50]. PECs are population coefficients of each species weighted by the respective Einstein coefficient for a transition to provide estimates of photon emissivity ($photons \cdot m^3 s^{-1}$). PECS are evaluated via equation (6)

$$\mathrm{PEC}\,(k,j) = A_{k,j}\frac{n_k}{n_e \sum_k n_k}. \tag{6}$$

$A_{k,j}$ is the Einstein coefficient for the $k \to j$ transition, n_k is the population density of state k. The atomic contributions to Balmer alpha emission are associated with atomic EIE and EIR, whilst the molecular contributions arise from the excited atoms formed from PMIs such as MAR, MAD, and MAI. Experimentally, a strong signature of the MAR and MAD processes is an increase in $D\alpha$ emission from excited deuterium atoms ($D(n=3)$) after D_2^+ interacts with the plasma. Therefore, figure 10 shows the various atomic (EIE and EIR) and molecular (mostly driven by D_2^+) contributions for the three different rate cases. These emission contributions are calculated based on the electron density, temperature, neutral atom density, molecular density and D_2^+ density, using a similar emission model as employed in [50], using Yacora on the Web [51] and ADAS [49] collisional-radiative modelling results for the molecular and atomic contributions to the $D\alpha$ emission, respectively. This method was selected because SOLPS-ITER calculates the emissivity of a cell by summing the contribution from the two bisecting EIRENE triangles within it, rather than averaging them. This approximately doubles the emissivity of each grid cell [50]. Figure 10 shows a marked increase in the atomic (mostly in EIR), and molecular contributions to Balmer alpha emission in the X1RED and X1EXT cases when compared to the AMJUEL case. In particular, the $D\alpha$ emission strongly increases in detached conditions for the X1RED and X1EXT cases, due to excited atoms after plasma-molecular interactions, which is qualitatively consistent with experimental results from MASTU and TCV [9, 10].

5. Discussion

The reduced and extended implementations of the Yacora $H_2(X^1, v)$ model have been used to calculate the vibrational distribution and thus from the cross-sections of the Yacora $H_2(X^1, v)$ model molecular effective rate coefficients. These coefficients were stored in EIRENE style databases

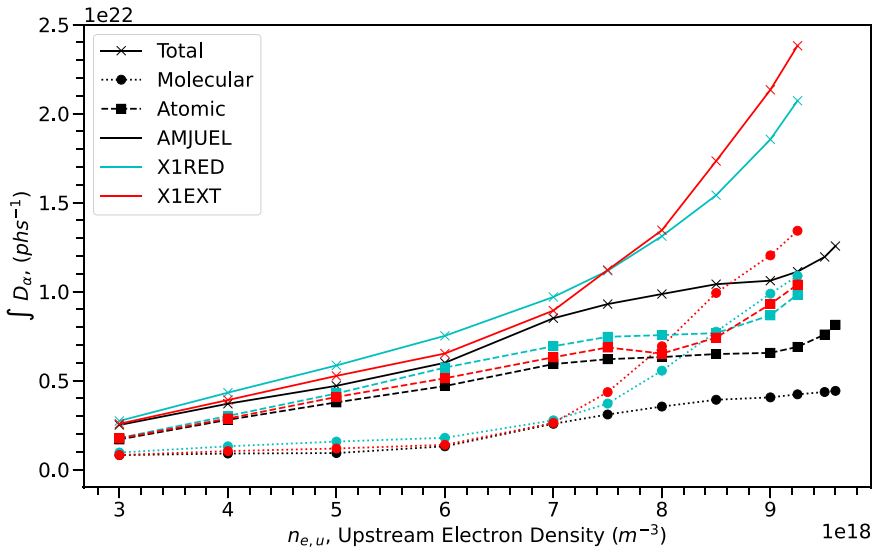

Figure 10. Comparison of line-integrated Balmer alpha emissions over the isolated leg domain. Total (solid), Molecular associated (dotted), and Atomic (dashed) emissions as a function of upstream heat flux density for the AMJUEL (black), X1RED (cyan), and X1EXT (red) cases. Atomic emissions were evaluated using Atomic PECs from ADAS [49]. The Molecular emission was evaluated using Yacora (on the web) Molecular PECs with the D_2 and D_2^+ densities provided through simulation [22, 50].

X1RED and X1EXT respectively. The reduced implementation employs the same interactions as EIRENE but with updated cross-sections and the extended implementation adds H_2^+ recombination, off-diagonal vibrational excitation through electron-impact, electronic excitation to higher order singlet states of H_2 and radiative decay. The improved cross-sections for MCX leads to a smoother decay at temperatures below $T_e < 1\,\text{eV}$. In addition, the introduction of off-diagonal transitions, transitions to electronic singlet states and H_2^+ recombination leads to an elevated population of the higher vibrational levels at low temperatures. This results in an increase in the MCX effective rate coefficient below $T_e < 0.5\,\text{eV}$ [11, 52]. At $T_e = 0.25\,\text{eV}$ this enhances the X1EXT MCX effective rate coefficient by a factor of ~ 100 compared to the X1RED effective rate coefficient. In simulation this increases the D_2^+ population, resulting in an increase of MAR by a factor of ~ 3 for the X1RED case and a factor ~ 4 for the X1EXT case, compared to the AMJUEL case. MAD increases by a factor of ~ 1.7 for the X1RED case and a factor of ~ 2. The increase of ion sinks reduces the detachment onset by approximately 9% and 16% for the X1RED and X1EXT cases, compared to the AMJUEL case, and results in a stronger reduction of ion flux due to MAR ion sinks. MAR and MAD increase the production of neutral D atoms, resulting in additional power losses and an increase in $D\alpha$ emission due to excited atoms after plasma-molecular interactions. Such power losses result in a reduction of the target temperature, which increases EIR in the X1EXT case once the plasma temperature drops below $T_e = 0.5\,\text{eV}$. The application of the Yacora $H_2(X^1, v)$ model to SOLPS-ITER results significant levels of MAR and MAD, impacting divertor power and particle balance as well as the $D\alpha$ emission. This is qualitatively consistent with observed experimental trends on MAST-U and TCV [11, 52].

5.1. Limitations of the Yacora $H_2(X^1, v)$ CR model

Although improvements in the molecular rate setup results in behaviour that is more consistent with experimental observations, there are limitations in the currently used molecular rate setup. Compared to AMJUEL, the electron density dependence of the, currently obtained, effective EID and NDI rate coefficients is potentially underestimated. For such interactions, AMJUEL employs the Sawada and Fujimoto [26] CR model, which is electronically resolved for both H_2 and H. This assumes a vibrational ground state, which is rescaled using a vibrational distribution from H2VIBR and an analytic model [21] to higher vibrational levels using an energy independent constants. This approach ignores the reduction of the energy threshold for EID for higher vibrational states, resulting in an underestimation of EID at low electron temperatures; which is improved upon in the used Yacora $H_2(X^1, v)$ setup. However, the AMJUEL implementation does account for processes that are important at increased electron densities, such as multi-step electronic excitation processes for H_2 (i.e. $e^- + H_2 \rightarrow e^- + H_2^*$, $e^- + H_2^* \rightarrow e^- + H_2^{**}$) and ionisation of excited atoms after dissociation (i.e. $e^- + H_2 \rightarrow e^- + H^* + H$, $e^- + H^* \rightarrow 2e^- + H^+$). The latter process effectively changes EID into NDI, thus leading to an electron density dependent balance between EID and NDI. In contrast, the currently employed model does not include these two processes, thus potentially underestimating their density dependence at high electron densities. Ideally, a fully self-consistent vibrationally and electronically resolved CR setup with multi-step processes where both excited levels of atoms and molecules are tracked simultaneously would be used to resolve such underestimations.

Other reactions, such as vibrational-vibrational exchange or vibrational excitation via proton collision are implemented

in the Yacora $H_2(X^1, v)$ model but have been deactivated for the application of this work [20]. These may alter the vibrational distribution [20]. Indeed, the observed vibrational distribution on MAST-U during detached conditions is inconsistent with the Boltzmann-like vibrational distributions obtained by H2VIBR, X1RED and X1EXT [53]. Additionally, the Yacora $H_2(X^1, v)$ model is not rotationally-resolved. The rotational distribution may impact certain interaction rates [25], such as EID [54]. To avoid the EIRENE mass-rescaling of ion-impact rates from hydrogen to deuterium and tritium, these rates should be calculated and stored independently as one cannot apply such mass-rescaling on an effective hydrogen rate correctly. Although this could have been corrected in this study, the EIRENE mass-rescaling for MCX was kept in place to keep the output consistent with the AMJUEL reference case. As mentioned previously, the incorrectly applied ion isotope mass-rescaling has likely reduced the difference between the AMJUEL and X1RED/X1EXT MCX rate coefficients. Additionally, chemical differences between the isotopes exist and the hydrogenic isotope have different energy levels for their vibrational states. To account for this, deuterium cross-sectional data is required either by using the hydrogen cross-sectional data with various assumptions or by having *ab initio* calculated data for deuterium. Presently, *ab initio* calculated data for deuterium cannot be sourced for all reactions included in the Yacora $H_2(X^1, v)$ model [20].

5.2. Limitations of the SOLPS-ITER application

Codes such as SOLPS-ITER employ effective rate coefficients that act on the molecular ground state density. Such an approach results in inherent assumptions: it assumes that transport of vibrationally excited molecules as well as interactions between such molecules and the wall can be negligible. However, such assumptions may not be valid in deeply detached plasmas. This would contradict the assumption in this paper that all vibrational levels of the molecular ground state are slowly evolving species, which is required for numerical validity in CR modelling [21]. In deeply detached conditions, the mean free path of vibrationally excited molecules can exceed the divertor size. This would imply that the time for the vibrational distribution to reach a quasi-steady state in time-dependent CR models may be longer than the transport time at low temperatures [55]. Additionally, interactions between the wall and vibrationally excited molecules can change the vibrational distribution [56]. These factors can increase the level of vibrational excitation in detached plasmas and boosting the levels of MAR and MAD. For example, electronic excitation in a moderately hot plasma ($T_e \approx 5$ eV) followed by radiative decay can boost higher vibrational states and those molecules can transport into a colder detached regime. Such behaviour can be studied by the comparison of vibrationally-resolved simulations to the vibrationally-unresolved results in this study.

The SOLPS-ITER application of additional reactions that are present in the Yacora $H_2(X^1, v)$ model need to be explored. The Yacora $H_2(X^1, v)$ model contains two dissociative ionisation reactions, one for the ionic ground state $H_2^+(^2\Sigma_g^+)$ state and the other for the repulsive ionic state $H_2^+(^2\Sigma_u^+)$. AMJUEL tracks an electronically and vibrationally unresolved H_2^+ species [14, 57]. The application of these rate coefficients will be important, however for clarity this work used the AMJUEL H.4 2.2.10 dissociative ionisation effective rate coefficient to isolate the effects of MCX, NDI and EID on detachment dynamics. Reactions that convert D_2^+ to D_2 such as D_2^+ radiative and 3-body recombination will decrease the D_2^+ population. Therefore, the impact of D_2^+ for the X1EXT case is likely overestimated in this study.

5.3. Outlook

To validate the X1EXT database further, a next step is to apply it to 2D experimental geometries and compare the modelling results against the experiment results, such as those obtained on MAST-U and TCV. Extrapolations of rate modifications to more reactor relevant conditions should be explored, as the effect of these rate coefficients on detachment may be less pronounced when applied to higher power devices such as STEP, ITER and EU-DEMO. These devices (may) employ divertors which have lower flux expansion, higher electron densities, and lower neutral confinement than the MAST Upgrade Super-X which could limit plasma-molecular interactions and lessen the impact of these rate coefficients when applied. Experimental evidence shows that when conventional divertors reach cold temperatures ($T_e < 1$ eV) EIR is the dominant recombination reaction as the divertor electron density present is higher, whilst the neutral densities are much lower than the MAST Upgrade Super-X divertor [58–60]. It is likely that ITER will follow this trend. Alternative divertors such as the snowflake, and X-point radiator may not have the volume necessary to replicate the radiating volume and neutral confinement seen in the MAST Upgrade Super-X for molecules to play a significant role in volume recombination and emission [61–64]. X-point target studies that combine the strike-point splitting of the snow-flake and the radial extent of the Super-X are ongoing on MAST Upgrade. It is a question whether molecules play an important role in this divertor geometry [65, 66]. To explore the reactor-relevancy of these molecular effective rate coefficients a first step could be to apply these effective rate coefficients to isolated divertor leg simulations with reactor-relevant levels of power input, and the presence of impurity radiators.

6. Conclusions

In this paper, it has been demonstrated that the use of newly calculated molecular rate coefficients based on the Yacora $H_2(X^1, v)$ collisional-radiative model (a reduced (X1RED) and 'extended' (X1EXT) implementation) has yielded stronger levels of plasma-molecular interactions when applied to an isolated divertor geometry in SOLPS-ITER with MAST Upgrade L-mode Super-X conditions. The improvements in the MCX rate in the X1RED and X1EXT databases significantly increase the levels of D_2^+. In deep detachment, the total D_2^+ population is roughly 40%–60% larger than in the

AMJUEL reference case. This results MAR increasing by a factor of ~ 3 and ~ 4 in the X1RED and X1EXT setups. MAD increases by a factor of ~ 1.75 and ~ 2 in the X1RED and X1EXT setups, respectively. These additional ion sinks reduce the onset of detachment by approximately 9% and 16% in the X1RED and X1EXT setups respectively, when compared to AMJUEL. Neutral production from MAR and MAD increases the neutral atom density and results in significant power losses, lowering the ion target flux. Such power losses result in lower electron temperatures, increasing the EIR ion sink for the X1EXT setup. This lower ion target flux is reminiscent of deeper detachment. The excited atoms born after MAR and MAD in the X1RED and X1EXT setups leads to an increase of $D\alpha$ emission after detachment.

Using the Yacora $H_2(X^1, v)$ model evaluated databases in the SOLPS-ITER isolated divertor setup [9, 10], instead of the AMJUEL reference rate coefficients, results in trends (increased ion sinks, stronger ion target flux roll-over, larger power dissipation from plasma-molecular interactions and an increase in $D\alpha$ emission during detachment) that are qualitatively in better agreement with experimental observations on TCV and MAST Upgrade.

Acknowledgment

The author would like to thank the staff at IPP Garching for their hospitality during this collaboration. This work received support from the EPSRC Grant EP/S022430/1. The data and models underlying this paper are available upon request. The Yacora solver is restricted to IPP Garching. The public model, Yacora on the web is available at (www.yacora.de).

ORCID iDs

J. Bryant https://orcid.org/0009-0000-1193-7972
K. McKay https://orcid.org/0000-0003-1822-7994
J.R. Harrison https://orcid.org/0000-0003-2906-5097
D. Moulton https://orcid.org/0009-0001-8439-9551
K. Verhaegh https://orcid.org/0000-0002-0500-2764
C. Cowley https://orcid.org/0000-0001-7065-8922
R.C. Bergmayr https://orcid.org/0000-0002-5851-0850
U. Fantz https://orcid.org/0000-0003-2239-3477
D. Wünderlich https://orcid.org/0000-0003-2810-9633

References

[1] Pitts R.A. *et al* 2019 Physics basis for the first ITER tungsten divertor *Nucl. Mater. Energy* **20** 100696
[2] Kirschner A. *et al* 2023 Erosion estimates for the divertor and main wall components from STEP *Nucl. Fusion* **63** 12
[3] Wenninger R. *et al* 2014 DEMO divertor limitations during and in between ELMs *Nucl. Fusion* **54** 114003
[4] Kallenbach A. *et al* 2013 Impurity seeding for tokamak power exhaust: from present devices via ITER to DEMO *Plasma Phys. Control. Fusion* **55** 124041
[5] Komm M. *et al* 2019 Divertor impurity seeding experiments at the COMPASS tokamak *Nucl. Fusion* **59** 106035
[6] Stangeby P. 1993 Can detached divertor plasmas be explained as self-sustained gas targets? *Nucl. Fusion* **33** 1695–703
[7] Cowley C., Lipschultz B., Moulton D. and Dudson B. 2022 Optimizing detachment control using the magnetic configuration of divertors *Nucl. Fusion* **62** 086046
[8] Lipschultz B. *et al* 1997 Modification and control of divertor detachment in Alcator C-Mod *J. Nucl. Mater.* **241–243** 771–6
[9] Verhaegh K. *et al* 2023 Spectroscopic investigations of detachment on the MAST Upgrade Super-X divertor *Nucl. Fusion* **63** 016014
[10] Verhaegh K. *et al* 2021 The role of plasma-molecule interactions on power and particle balance during detachment on the TCV tokamak *Nucl. Fusion* **61** 106014
[11] Verhaegh K. *et al* 2023 Investigating the impact of the molecular charge-exchange rate on detached SOLPS-ITER simulations *Nucl. Fusion* **63** 076015
[12] Wiesen S. *et al* 2015 The new SOLPS-ITER code package *J. Nucl. Mater.* **463** 480–4
[13] Braginskii S.I. 1965 Transport processes in a plasma *Rev. Plasma Phys.* **1** 205–311
[14] Reiter D. 2019 EIRENE manual (available at: www.eirene.de/old_eirene/eirene.pdf)
[15] Moulton D. *et al* 2024 Super-X and conventional divertor configurations in MAST-U ohmic L-mode; a comparison facilitated by interpretative modelling *Nucl. Fusion* **64** 076049
[16] Ichihara A., Iwamoto O. and Janev R.K. 2000 Cross sections for the reaction $H^+ + H_2$ ($v = 0 - 14$) $\rightarrow H + H_2^+$ at low collision energies *J. Phys. B: At. Mol. Opt. Phys.* **33** 4747–58
[17] Janev R.K., Reiter D. and Samm U. 2003 Collision processes in low-temperature hydrogen plasmas *Juel-Report 4105* Forschungszentrum Juelich (available at: https://juser.fz-juelich.de/record/38224/files/Juel_4105_Reiter.pdf)
[18] Errea L.F., Fernández L., Méndez L., Pons B., Rabadán I. and Riera A. 2007 Vibronic treatment of vibrational excitation and electron capture in $H^+ + H_2$ (HD, D2,...) collisions at low impact energies *Phys. Rev.* A **75** 032703
[19] Urbain X. *et al* 2013 New light shed on charge transfer in fundamental $H^+ + H_2$ collisions *Phys. Rev. Lett.* **111** 203201
[20] Bergmayr R.C., Wünderlich D. and Fantz U. 2023 Molecular data needs for advanced collisional-radiative modelling for hydrogen plasmas *Eur. Phys. J.* D **77** 136
[21] Greenland P.T. 2001 Collisional-radiative models with molecules *Proc. R. Soc.* A **457** 1821–39
[22] Wünderlich D., Giacomin M., Ritz R. and Fantz U. 2020 Yacora on the web: online collisional radiative models for plasmas containing H, H_2 or He *J. Quant. Spectrosc. Radiat. Transfer* **240** 106695
[23] Capitelli M., Celiberto R. and Cacciatore M. 1994 Needs for cross sections in plasma chemistry *Adv. At. Mol. Opt. Phys.* **33** 321–72
[24] Kushnir D., Waxman E. and Chugunov A.I. 2019 Screening of fusion reactions from the principle of detailed balance and application to the pep reaction *Mon. Not. R. Astron. Soc.* **486** 449–52
[25] Sawada K. and Goto M. 2016 Rovibrationally resolved time-dependent collisional-radiative model of molecular hydrogen and its application to a fusion detached plasma *Atoms* **4** 29
[26] Sawada K. and Fujimoto T. 1995 Effective ionization and dissociation rate coefficients of molecular hydrogen in plasma *J. Appl. Phys.* **78** 2913–24
[27] Reiter D. 2020 AMJUEL database (available at: www.eirene.de/Documentation/amjuel.pdf)
[28] Holm A., Börner P., Rognlien T.D., Meyer W.H. and Groth M. 2021 Comparison of a collisional-radiative fluid model of

H2 in UEDGE to the kinetic neutral code EIRENE *Nucl. Mater. Energy* **27** 100982
[29] Cianfrani F., Borodin D.V. and Küppers B. 2023 Data processing and visualization tool for atomic and molecular data for collisional radiative models *Eur. Phys. J.* D **77** 139
[30] Karhunen J. *et al* 2022 Inference of molecular divertor density from filtered camera analysis of molecularly induced Balmer line emission during detachment in JET L-mode plasmas *J. Instrum.* **17** 075001
[31] Fantz U., Reiter D., Heger B. and Coster D. 2001 Hydrogen molecules in the divertor of ASDEX Upgrade *J. Nucl. Mater.* **290–293** 367–73
[32] Havlíçková E., Fundamenski W., Wischmeier M., Fishpool G. and Morris A.W. 2014 Investigation of conventional and Super-X divertor configurations of MAST Upgrade using scrape-off layer plasma simulation *Plasma Phys. Control. Fusion* **56** 075008
[33] Havlíčková E. *et al* 2015 SOLPS analysis of the MAST-U divertor with the effect of heating power and pumping on the access to detachment in the Super-X configuration *Plasma Phys. Control. Fusion* **57** 115001
[34] Samm U. 2005 Plasma—wall interaction: status and data needs *Nuclear Fusion Research* (*Springer Series in Chemical Physics* vol 78) 1st edn, ed R.E. Clark and D.H. Reiter (Springer) pp 3–28
[35] Kotov V., Reiter D. and Kukushkin A.S. 2007 Numerical study of the ITER divertor plasma with the B2-EIRENE code package *Juel-Report* 4257 Forschungszentrum Juelich
[36] Fantz U. and Wünderlich D. 2014 Fundamental data of diatomic molecules relevant for fusion 56–72 (available at: www.iaea.org/publications/8475/atomic-and-plasma-material-interaction-data-for-fusion)
[37] Greenland P. 2001 The CRMOL manual: collisional-radiative models for molecular hydrogen in plasmas (available at: https://juser.fz-juelich.de/record/24992/files/J%C3%BCl_3858_Greenland.pdf?version = 1)
[38] Janev R.K., Langer W.D., Post D.E. and Evans K. 1987 *Elementary Processes in Hydrogen-Helium Plasmas*
[39] Scarlett L., Savage J., Fursa D., Zammit M. and Bray I. 2019 Electron-impact dissociation of vibrationally-excited molecular hydrogen into neutral fragments *Atoms* **7** 75
[40] Fantz U. 2006 Basics of plasma spectroscopy *Plasma Sources Sci. Technol.* **15** S137
[41] Moulton D., Harrison J., Lipschultz B. and Coster D. 2017 Using SOLPS to confirm the importance of total flux expansion in Super-X divertors *Plasma Phys. Control. Fusion* **59** 065011
[42] Eckstein W. and Heifetz D.B. 1987 Data sets for hydrogen reflection and their use in neutral transport calculations *J. Nucl. Mater.* **145-147** 332–8
[43] Pshenov A.A., Kukushkin A.S. and Krasheninnikov S.I. 2017 Energy balance in plasma detachment *Nucl. Mater. Energy* **12** 948–52
[44] Reiter D., May C., Baelmans M. and Börner P. 1997 Non-linear effects on neutral gas transport in divertors *J. Nucl. Mater.* **241–243** 342–8
[45] Wu H., Subba F., Wischmeier M. and Zanino R. 2020 Comparison of SOLPS5.0 and SOLPS-ITER simulations for ASDEX Upgrade L-mode *Contrib. Plasma Phys.* **60** 4
[46] Kotov V., Reiter D., Coster D.P. and Kukushkin A.S. 2010 Verification of the 2D tokamak edge modelling codes for conditions of detached divertor plasma *Contrib. Plasma Phys.* **50** 292–8
[47] Stangeby P. 2020 The roles of power loss and momentum-pressure loss in causing particle-detachment in tokamak divertors: I. A heuristic model analysis *Plasma Phys. Control. Fusion* **62** 025012
[48] Dudson B.D. *et al* 2019 The role of particle, energy and momentum losses in 1D simulations of divertor detachment *Plasma Phys. Control. Fusion* **61** 065008
[49] Guzmán F., O'Mullane M. and Summers H.P. 2013 ADAS tools for collisional-radiative modelling of molecules *J. Nucl. Mater.* **438** S585–8
[50] Verhaegh K. *et al* 2021 A novel hydrogenic spectroscopic technique for inferring the role of plasma-molecule interaction on power and particle balance during detached conditions *Plasma Phys. Control. Fusion* **63** 035018
[51] Wünderlich D. *et al* 2021 Application of molecular convergent close-coupling cross sections in a collisional radiative model for the triplet system of molecular hydrogen *J. Phys. D: Appl. Phys.* **54** 115201
[52] Verhaegh K. *et al* 2023 The role of plasma-atom and molecule interactions on power & particle balance during detachment on the MAST Upgrade Super-X divertor *Nucl. Fusion* **63** 126023
[53] Osborne N. *et al* 2024 Initial Fulcher band observations from high resolution spectroscopy in the MAST-U divertor *Plasma Phys. Control. Fusion* **66** 025008
[54] Fabrikant I.I., Wadhera J.M. and Xu Y. 2002 Resonance processes in e−H2 collisions: dissociative attachment and dissociation from vibrationally and rotationally excited states *Phys. Scr.* **T96** 45
[55] Kobussen S. 2023 Collisional radiative modelling with improved cross sections to investigate plasma molecular interactions in divertor plasmas (arXiv:2311.16732)
[56] Saito S., Nakamura H., Sawada K., Kawamura G., Kobayashi M. and Hasuo M. 2020 Molecular dynamics simulation model of hydrogen recycling on carbon divertor for neutral transport analysis in large helical device *Contrib. Plasma Phys.* **60** e201900152
[57] Sawada K., Yamada Y., Miyachika T., Ezumi N., Iwamae A. and Goto M. 2010 Collisional-radiative model for spectroscopic diagnostic of optically thick helium plasma *Plasma Fusion Res.* **5** 001
[58] Terry J.L. *et al* 1999 Experimental determination of the volume recombination rate in tokamak divertors *J. Nucl. Mater.* **266** 30–36
[59] McCracken G.M. *et al* 1999 Volume recombination and detachment in JET divertor plasmas *J. Nucl. Mater.* **266** 37–43
[60] Wenzel U. *et al* 1999 Volume recombination in divertor I of ASDEX Upgrade *Nucl. Fusion* **39** 873
[61] Pan O. *et al* 2023 SOLPS-ITER simulations of an X-point radiator in the ASDEX Upgrade tokamak *Nucl. Fusion* **63** 016001
[62] Bernert M. *et al* 2023 The X-point radiating regime at ASDEX Upgrade and TCV *Nucl. Mater. Energy* **34** 101376
[63] Soukhanovskii V.A., Cunningham G., Harrison J.R., Federici F. and Ryan P. 2022 First snowflake divertor experiments in MAST-U tokamak *Nucl. Mater. Energy* **33** 101278
[64] Labit B. *et al* 2017 Experimental studies of the snowflake divertor in TCV *Nucl. Mater. Energy* **12** 1015–9
[65] Umansky M.V. *et al* 2017 Assessment of X-point target divertor configuration for power handling and detachment front control *Nucl. Mater. Energy* **12** 918–23
[66] Cowley C. *et al* 2023 Novel SOLPS-ITER simulations of X-point target and snowflake divertors *Plasma Phys. Control. Fusion* **65** 035011